

A guided ion beam investigation of  $\text{UO}_2^+$  thermodynamics and f orbital participation: Reactions of  $\text{U}^+ + \text{CO}_2$ ,  $\text{UO}^+ + \text{O}_2$ , and  $\text{UO}^+ + \text{CO}$

Amanda R. Bubas, Wen-Jing Zhang,<sup>a</sup> and P. B. Armentrout\*

Department of Chemistry, University of Utah, 315 S 1400 E Rm 2020, Salt Lake City, UT 84112-0850, USA

#### ABSTRACT

A guided ion beam tandem mass spectrometer (GIBMS) was employed to study the reactions of  $\text{U}^+ + \text{CO}_2$ ,  $\text{UO}^+ + \text{O}_2$ , and the reverse of the former,  $\text{UO}^+ + \text{CO}$ . Reaction cross sections as a function of kinetic energy over about a three order of magnitude range were studied for all systems. The reaction of  $\text{U}^+ + \text{CO}_2$  proceeds to form  $\text{UO}^+ + \text{CO}$  with an efficiency of  $118 \pm 24\%$  as well as generating  $\text{UO}_2^+ + \text{C}$  and  $\text{UCO}^+ + \text{O}$ . The reaction of  $\text{UO}^+ + \text{O}_2$  forms  $\text{UO}_2^+$  in an exothermic, barrierless process, and also results in the collision-induced dissociation (CID) of  $\text{UO}^+$  to yield  $\text{U}^+$ . In the  $\text{UO}^+ + \text{CO}$  reaction, formation of  $\text{UO}_2^+$  in an endothermic process is the dominant reaction, but minor products of  $\text{UCO}^+ + \text{O}$  and  $\text{U}^+ + (\text{O} + \text{CO})$  are also observed. Analysis of the kinetic energy dependences observed provides the bond energies,  $D_0(\text{U}^+-\text{O}) = 7.98 \pm 0.22$  eV,  $D_0(\text{U}^+-\text{CO}) = 0.52 \pm 0.29$  eV, and  $D_0(\text{OU}^+-\text{O}) = 7.56 \pm 0.12$  eV. The values obtained for  $D_0(\text{U}^+-\text{O})$  and  $D_0(\text{OU}^+-\text{O})$  agree well with previously reported literature values. To our knowledge, this is the first experimental measurement of  $D_0(\text{U}^+-\text{CO})$ . An analysis of the oxide bond energies shows that participation of 5f orbitals leads to a substantial increase in the thermodynamic stability of  $\text{UO}_2^+$  relative to  $\text{ThO}_2^+$  and especially transition metal dioxide cations.

**Corresponding Author:** \*P. B. Armentrout; email: [armentrout@chem.utah.edu](mailto:armentrout@chem.utah.edu)

<sup>a</sup> Present address: Department of Chemistry, Texas A & M University, College Station, TX 77843

ACCEPTED MANUSCRIPT

The Journal of  
Chemical PhysicsAIP  
Publishing

This is the author's peer reviewed, accepted manuscript. However, the online version of record will be different from this version once it has been copyedited and typeset.

PLEASE CITE THIS ARTICLE AS DOI: 10.1063/5.0183836

## INTRODUCTION

The actinides remain the subjects of experimental and computational studies because of their applications in nuclear fuel systems. Because of the radioactivity associated with the actinide elements, many of them are difficult to study experimentally. The least radioactive actinides, thorium and uranium, offer a safer route to directly examine actinide chemistry, which can provide experimental benchmark data that can be used to evaluate computational models. Computations serve as a viable method to explore the fundamental chemistry of transuranics that cannot easily be studied experimentally. Gas-phase studies offer the unique opportunity to study the actinides free of solvent effects, thereby enabling a more direct comparison to computational models.

Several gas-phase studies have shared the objective of gathering thermodynamic information for uranium oxide species. Armentrout and Beauchamp (AB) studied the reactions of  $U^+$  and  $UO^+$  with  $O_2$ ,  $CO$ ,  $CO_2$ ,  $COS$ ,  $CS_2$ , and  $D_2O$  using an early ion beam mass spectrometer.<sup>1</sup> The reactions of  $U^+ + O_2$  and  $UO^+ + O_2$  yielded  $UO^+$  and  $UO_2^+$ , respectively in exothermic, barrierless processes. The reaction of  $U^+ + O_2$  proceeded at a thermal rate of  $5.6 \times 10^{-10} \text{ cm}^3/\text{sec}$ . Reaction of  $U^+$  with  $CO$  formed both  $UO^+$  and  $UC^+$  in endothermic processes. The reaction of  $U^+ + CO_2$  resulted primarily in the exothermic formation of  $UO^+ + CO$ , and the reaction of  $UO^+ + CO_2$  yielded  $UO_2^+$ . Although the latter reaction was expected to be exothermic by  $\sim 2.3 \text{ eV}$ , the  $UO_2^+$  cross section displayed an endothermic feature, indicating an energy barrier of  $1.3 \pm 0.1 \text{ eV}$ . AB suggested that a potential energy surface crossing could explain the reaction barrier. AB subsequently conducted collision-induced dissociation (CID) experiments of  $UO^+ + Ar$  and  $UO_2^+ + Ar$  to directly measure  $D_0(U^+-O)$  and  $D_0(UO^+-O)$  and obtained values of  $8.0 \pm 0.3 \text{ eV}$  and  $7.7 \pm 0.4 \text{ eV}$ , respectively.<sup>2</sup>

Andrews and coworkers recorded infrared (IR) spectra for products resulting from reactions of uranium atoms and cations with  $O_2$  in an argon matrix.<sup>3</sup> They were able to characterize the resulting product and proposed an insertion mechanism for the formation of  $UO_2$ . They later recorded the IR spectra of  $UO_2$ ,  $UO_2^+$ , and  $UO_2^-$  in a neon matrix and performed density functional theory (DFT) calculations to obtain vibrational frequencies, identify low-lying electronic states,

assess relative energies, and visualize geometries for the observed dioxide products.<sup>4</sup> Here, the ground electronic state of  $\text{UO}_2^+$  was identified as  $^2\Phi_u$ , although the  $^2\Delta_u$  state was calculated to be only 0.22 eV higher in energy.

Nitsche et al. performed ab initio calculations to examine structural and bonding characteristics of  $\text{UO}_2^{2+}$ ,  $\text{UO}_2^+$ ,  $\text{UO}_2$ ,  $\text{UO}_2^-$ ,  $\text{OUCO}^-$ ,  $\text{O}_2\text{U}(\text{CO})_2$ , and  $\text{UO}_2\text{CO}_3$ .<sup>5</sup> Extensive theoretical calculations used in this study included B3LYP, Møller-Plesset perturbation (MP2), coupled cluster doubles (CCD), complete active space multiconfiguration self-consistent field (CASMCSCF), and multireference singles and doubles configuration interaction (MRSDCI). All levels of theory employed identified a  $^3\Phi_u$  ground electronic state for  $\text{UO}_2$  and a  $^2\Phi_u$  ground electronic state for  $\text{UO}_2^+$  and indicated that  $\text{UO}_2$  and  $\text{UO}_2^+$  are linear molecules, in agreement with previous experimental and DFT results from Andrews and coworkers.

Heaven and coworkers employed resonantly enhanced multiphoton ionization (REMPI) to measure the ionization energies (IEs) of  $\text{UO}$  and  $\text{UO}_2$  and to probe the electronic structure of  $\text{UO}_2$ .<sup>6</sup> The IEs obtained for  $\text{UO}$  and  $\text{UO}_2$  were  $6.0313 \pm 0.0006$  eV and  $6.128 \pm 0.003$  eV, respectively. The ground electronic state of  $\text{UO}_2$  was determined to be  $^3\Phi_u$  with a configuration of  $\text{U}(5f\phi_u 7s\sigma_g)\text{O}_2$ . A later computational study by Gagliardi et al. provided additional support for the experimental spectral assignments and a  $^3\Phi_u$  ground state.<sup>7</sup> The electronic structures of  $\text{UO}^+$  and  $\text{UO}_2^+$  were further studied using pulsed-field ionization zero electron kinetic energy (PFI-ZEKE) spectroscopy.<sup>8-9</sup> This study refined  $\text{IE}(\text{UO})$  to  $6.031065 \pm 0.000025$  eV and supported a  $\text{U}^{3+}(5f^3)\text{O}^{2-}$  configuration as the  $\text{UO}^+$  ground state. It also provided  $\text{IE}(\text{UO}_2) = 6.127 \pm 0.001$  eV and supported a  $\text{U}(5f\phi)\text{O}_2^+$  ( $^2\Phi_u$ ) ground state configuration.

More recently, Marçalo and Gibson reviewed and assessed experimental thermochemical values available for the actinide oxides.<sup>10</sup> Among the most relevant for the present study are the recommended values  $D_{298}(\text{U}-\text{O}) = 7.86 \pm 0.13$  eV,  $D_{298}(\text{U}^+-\text{O}) = 8.02 \pm 0.13$  eV,  $D_{298}(\text{OU}-\text{O}) = 7.77 \pm 0.15$  eV, and  $D_{298}(\text{OU}^+-\text{O}) = 7.68 \pm 0.15$  eV. We adjust these values to 0 K bond dissociation energies (BDEs) using the values determined by Kovacs et al. (0.06 eV for  $\text{UO}$  and 0.05 eV for  $\text{UO}_2$ ).<sup>11</sup> We assume the analogous cations have the same enthalpy corrections, leading

to  $D_0$  values of 7.80, 7.96, 7.72, and 7.63 eV, respectively. The increased availability of experimental data for the actinides has led to significant improvements in the accuracy of computational models used to describe the actinide elements. Zhang and Cheng recently performed a rigorous series of benchmark spinor-based relativistic coupled-cluster calculations for the IEs of U, UO, and  $\text{UO}_2$  as well as the BDEs of UO,  $\text{UO}^+$ ,  $\text{OU-O}$ , and  $\text{OU}^+\text{-O}$ .<sup>12</sup> They included a thorough assessment of the contributions from spin-orbit effects, electron correlation, and basis set and determined that calculations employing the CCSD(T) method with extrapolation to the complete basis set (CBS) limit provides excellent agreement with the experimentally obtained values.

The most recent and most direct measurement of the  $\text{U}^+\text{-O}$  bond dissociation energy (BDE) was reported by Zhang et al.<sup>13</sup> They utilized a guided ion beam tandem mass spectrometer (GIBMS) to study the energy dependence of the reactions of  $\text{U}^+ + \text{O}_2$  and  $\text{U}^+ + \text{CO}$ . The 0 K  $\text{UO}^+$  BDE obtained from their experimental results was  $7.88 \pm 0.09$  eV, consistent with their recommended value of  $8.01 \pm 0.13$  eV. (This value was obtained as the average of recommended values for  $D_0(\text{UO})$  from Pedley and Marshall<sup>14</sup> and Konings et al.,<sup>15</sup> leading to  $7.86 \pm 0.13$  eV, combined with the precisely determined ionization energies of U and UO by Heaven and co-workers.<sup>8</sup>) Here, we extend that work by exploring the reactions of  $\text{U}^+ + \text{CO}_2$ ,  $\text{UO}^+ + \text{O}_2$ , and  $\text{UO}^+ + \text{CO}$  using a GIBMS. The reaction of  $\text{U}^+ + \text{CO}_2$  proceeds with high efficiency to exothermically yield  $\text{UO}^+$  but also forms  $\text{UCO}^+$  and  $\text{UO}_2^+$  in endothermic processes. The reaction of  $\text{UO}^+ + \text{O}_2$  yields  $\text{UO}_2^+$  in an exothermic process and  $\text{U}^+$  in an endothermic process. The study of the related reaction of  $\text{UO}^+ + \text{CO}$  yields  $\text{UO}_2^+$ ,  $\text{UCO}^+$ , and  $\text{U}^+$ , all in endothermic processes. Analysis of the kinetic energy dependences of these various reactions provides direct measurements of the threshold energies for  $\text{U}^+$ ,  $\text{UCO}^+$ , and  $\text{UO}_2^+$  formation, from which  $D_0(\text{U}^+\text{-O})$ ,  $D_0(\text{U}^+\text{-CO})$ , and  $D_0(\text{OU}^+\text{-O})$  and the corresponding reaction thermochemistry can be determined.

## EXPERIMENTAL METHODS

*Instrument*

The GIBMS employed in these experiments has been described in detail previously,<sup>16</sup> therefore only a brief overview is provided here. A direct current (DC) discharge ion source was used to generate bare uranium cations from a uranium cathode.<sup>17</sup> These ions then underwent  $\sim 10^5$  thermalizing collisions with a helium/argon (90/10) mixture in a meter long flow tube (FT). As detailed in previous work, the DC/FT source has been used to generate atomic transition metal cations with internal energies characterized by effective temperatures of 300 – 1100 K.<sup>18-23</sup> For  $U^+$  at 300 K, 76% are in its ground level ( $^4I_{9/2}, 5f^3 7s^2$ ) and 23% in its first excited level ( $^6L_{11/2}, 5f^3 6d 7s$ ) at 0.036 eV.<sup>24-25</sup> At 1100 K, these populations change to 43% and 35% with additional contributions of 13%, 6%, and 3% in excited levels ( $^6K_{9/2}, 5f^3 6d 7s$ ), ( $^6L_{13/2}, 5f^3 6d 7s$ ), and ( $^6K_{11/2}, 5f^3 6d 7s$ ) at 0.113, 0.217, and 0.285 eV, respectively. Taking a conservative temperature to be  $700 \pm 400$  K, the  $U^+$  has an average electronic energy,  $E_{el}$ , of  $0.03 \pm 0.02$  eV.<sup>26</sup>

To create the  $UO^+$  reactant, the bare  $U^+$  cations were exposed to  $O_2$   $\sim 25$  cm downstream from the ion source. These ions then underwent  $\sim 10^5$  thermalizing collisions with a helium/argon (90/10) mixture in the remaining 75 cm of the flow tube (FT). For the  $UO^+$  reactant, the thermalization should be sufficient to form it in its ground electronic state.

After exiting the DC/FT source, the precursor ions were focused through a series of lenses and mass selected using a magnetic momentum analyzer.<sup>16</sup> The precursor ions of interest were then recollimated and injected into a radio frequency (rf) octopole ion guide, which is advantageous for its radial trapping efficiency. The octopole passed through a reaction cell containing the neutral reagent of interest ( $CO_2$ ,  $O_2$ , or  $CO$ ). The pressure of the neutral reagent was kept sufficiently low to maintain single collision conditions. Each reaction was also carried out at multiple pressures between 0.1 and 0.4 mTorr to allow for extrapolation to zero pressure, rigorously single collision conditions.<sup>27</sup> Foreground scans were collected with the neutral reagent directed into the reaction cell, and background scans were collected with the neutral reagent directed to the chamber surrounding the reaction cell so that background noise and signal resulting

from reactions outside of the collision cell could be explicitly subtracted. Precursor and product ions were extracted from the octopole for mass analysis by a quadrupole mass filter and detection using a Daly type detector.<sup>28</sup>

### Data Analysis

Raw data are ion intensities as a function of ion energy in the laboratory frame ( $E_{\text{Lab}}$ ), which are converted to cross sections as a function of energy in the center-of-mass frame ( $E_{\text{CM}}$ ).<sup>29</sup> The product ion intensities are first background subtracted and converted to cross sections,  $\sigma$ , using the equation,  $I = I_0 \exp(-\rho\sigma l)$ , where  $I$  is the intensity of the precursor ion after reaction,  $I_0$  is precursor intensity before reaction (assumed to equal  $I + \sum I_P$  where  $I_P$  are intensities of the various product ions),  $\rho$  is the number density of the neutral reactant, and  $l$  is the length of the collision cell (8.26 cm effective length). Uncertainties in the absolute cross section magnitudes are  $\pm 20\%$ .

The absolute zero of the energy scale is routinely determined by monitoring the intensity of the precursor ion while the DC voltage of the octopole is varied through the nominal zero of the ion kinetic energy. This produces a retarding potential curve, and the first derivative of this curve provides the ion energy distribution where the peak of the distribution corresponds to the absolute zero of the energy scale. Full widths at half maximum (FWHM) of the ion energy distribution were typically 0.5 – 0.6 eV (Lab), and uncertainties in the absolute energy scale are  $\pm 0.1$  eV (Lab). Lab frame energies were converted to center-of-mass frame energies by the equation  $E_{\text{CM}} = E_{\text{Lab}} \times m/(m + M)$ , where  $m$  is the mass of the neutral  $\text{CO}_2$ ,  $\text{O}_2$ , or  $\text{CO}$  reagent and  $M$  is the mass of the precursor ion,  $\text{U}^+$  or  $\text{UO}^+$ . At very low energies, the average energy of the reactant ions is corrected for truncation of the energy distribution. All energies are reported in the center-of-mass scale below.

Cross sections of endothermic reactions were modeled according to a modified line-of-centers (MLOC) model, Equation 1,<sup>30-33</sup>

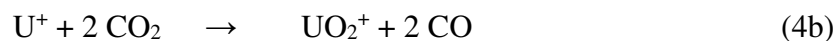
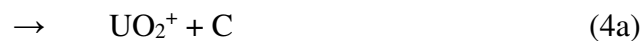
$$\sigma(E) = \sigma_0 \sum g_i (E + E_i + E_{el} - E_0)^n / E \quad (1)$$

where  $E$  is the relative kinetic energy of the reactants ( $E_{CM}$ ),  $\sigma_0$  is an energy independent scaling factor,  $E_i$  are the energies of rovibrational states of  $UO^+$ ,  $CO_2$ ,  $O_2$ , or  $CO$  reactants having populations  $g_i$  ( $\sum g_i = 1$ ),  $E_{el}$  is the electronic energy of the reactant ion,  $E_0$  is the reaction threshold, and  $n$  is an adjustable parameter that guides the shape of the model. At higher energies, a statistical model detailed elsewhere<sup>34</sup> was used to model product dissociation. The statistical model includes the parameters  $p$  and  $E_D$ , where  $p$  is similar to  $n$ , although can hold only integer values, and  $E_D$  is the energy at which product dissociation begins, generally close in value to the bond energy of the reactant neutral. Parameters in Eq. 1 and the high energy model were optimized to best reproduce the data using a nonlinear least squares analysis. Parameters for the high energy model were chosen such that they did not influence the model in the threshold region. Uncertainties were determined by variations associated with modeling multiple data sets, combined with uncertainties in the kinetic energy scale and internal energies of the reactants.

## EXPERIMENTAL RESULTS

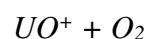
### $U^+ + CO_2$

The product ion cross sections as a function of ion kinetic energy for the reaction of  $U^+$  and  $CO_2$  are shown in Figure 1. The processes observed for the reaction of  $U^+$  and  $CO_2$  include:

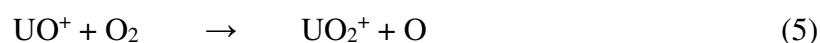


At low energies ( $< 1$  eV), the dominant product observed is  $UO^+$ , which is clearly formed in an exothermic, barrierless process. The magnitude of this cross section is pressure independent. Below  $\sim 0.5$  eV,  $UO_2^+$  is also observed with a cross section about three orders of magnitude smaller than that for reaction 2. This cross section then increases appreciably as the collision energy is increased and then rises more rapidly starting near 5 eV until it reaches a peak near 8 eV and declines sharply at higher energies. The  $UO_2^+$  cross section displays a linear dependence on  $CO_2$

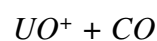
pressure at low energies (< 4 eV), indicating that this product is formed in the secondary process 4b. At higher energies, the  $\text{UO}_2^+$  cross section is pressure independent and thus is formed by reaction 4a. The  $\text{UCO}^+$  cross section (pressure independent) rises from a threshold of about 4.5 eV and then near 7 eV, the  $\text{UCO}^+$  cross section declines sharply.



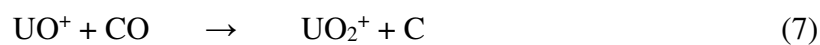
The product ion cross sections for the reaction of  $\text{UO}^+$  and  $\text{O}_2$  are shown in Figure 2 and include reactions 5 and 6.



Neither of the product ion cross sections display a pressure dependence, indicating they correspond to primary processes. The  $\text{UO}_2^+$  cross section dominates the products and this product is clearly formed in an exothermic, barrierless reaction. The much smaller  $\text{U}^+$  cross section rises from a threshold near 8 eV, consistent with the  $\text{UO}^+$  bond energy in the literature. Therefore, this process can be identified as simple collision-induced dissociation.



The product ion cross sections for the reaction of  $\text{UO}^+$  and  $\text{CO}$  are shown in Figure 3. The processes observed for the reaction of  $\text{UO}^+$  and  $\text{CO}$  include:



None of the product ion cross sections display a pressure dependence, therefore all products are the result of primary processes. The  $\text{UO}_2^+$  cross section has a small exothermic tail before rising near 3 eV and then declining after 10 eV. The tail at low energies is an artifact of a persistent  $\text{O}_2$  contaminant, which appears to be present at only a concentration of 0.010%. This is demonstrated by comparison of the absolute magnitudes of the  $\text{UO}^+ + \text{O}_2$  cross section shown in Figure 2 and the low-energy tail in Figure 3. The  $\text{UCO}^+$  cross section begins near 7 eV and then declines above

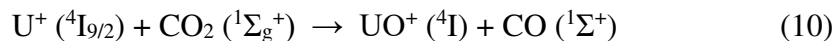
about 10 eV. The  $U^+$  cross section displays two distinct features. The initial rise in the  $U^+$  cross section occurs near 4 eV, with a second rise beginning near 8 eV. The initial rise can be attributed to process 9a, and the second rise can be attributed to collision-induced dissociation of  $UO^+$ , process 9b.

## DISCUSSION

### Reaction of $U^+ + CO_2$

#### *UO<sup>+</sup> product*

$UO^+$  is formed in an exothermic, barrierless reaction between  $U^+$  and  $CO_2$ , process 2, with high efficiency, shown in Figure 1. The high reaction efficiency can be attributed to the exothermicity of  $UO^+$  formation,  $\Delta_r H(2) = -2.47 \pm 0.13$  eV, as calculated using  $D_0(UO^+) = 8.01 \pm 0.13$  eV<sup>13</sup> and  $D_0(OC=O) = 5.543 \pm 0.001$  eV.<sup>35</sup> If we convert the cross section measured at the lowest energy (0.05 eV for six data sets) to a rate constant,  $k_2$ , we measure an average value of  $(5.2 \pm 1.0) \times 10^{-10}$  cm<sup>3</sup>/sec. Within experimental uncertainty, this matches the collision rate provided by the Langevin-Gioumousis-Stevenson expression,  $k_{LGS}$ , for the  $U^+ + CO_2$  reaction of  $4.4 \times 10^{-10}$  cm<sup>3</sup>/s.<sup>36-37</sup> The  $UO^+$  cross section then declines somewhat more rapidly (as  $E^{-0.78 \pm 0.02}$ ) than expected for the collision cross section ( $\sigma_{LGS}$  declines as  $E^{-0.5}$ ). We believe this may be a consequence of the mixture of  $U^+$  states formed in our DC/FT ion source. The  $U^+$  ground level can react with  $CO_2$  according to reaction 10 to form ground state  $UO^+$  ( $^4I$ ), whereas the reactions of low-lying sextet states of  $U^+$  are spin-forbidden.



Although spin would ordinarily not be expected to be a valid quantum number for such a heavy element, the spin restriction still means that reactions of the sextet states of  $U^+$  must undergo a surface crossing to form ground state  $UO^+$ . In the past, such spin-restrictions have been observed to be accompanied by an energy dependence of  $E^{-1/2}$ ,<sup>38-46</sup> which combined with the energy dependence of  $\sigma_{LGS}$  would lead to a decline in the cross section of  $E^{-1}$ . Because both  $U^+$  ( $^4I_{9/2}$ ) and  $U^+$  ( $^6L,K$ ) are believed to be present, the combination of spin-allowed ( $E^{-1/2}$ ) and spin-forbidden ( $E^{-1}$ ) pathways could lead to the observed energy dependence.

At energies above  $\sim 1$  eV, the  $\text{UO}^+$  cross section levels out, resembling the hard-sphere (HS) collision cross section,  $\sigma_{\text{HS}}$ , which we estimate as  $52 \text{ \AA}^2$  given a C=O bond length of  $1.162 \text{ \AA}$ ,<sup>47</sup> a  $\text{U}^+$  radius of  $1.38 \text{ \AA}$ ,<sup>48-49</sup> and O van der Waals radius of  $1.52 \text{ \AA}$ .<sup>48</sup> The sharp decline in the  $\text{UO}^+$  cross section after 8 eV indicates decomposition of the  $\text{UO}^+$  product. In reaction 2,  $\text{UO}^+$  product dissociation can begin at  $5.543 \text{ eV} = D_0(\text{OC}=\text{O})$ . The observation that dissociation is delayed to higher energies indicates that the neutral CO product carries away some of the energy available to the products.

The behavior of the  $\text{UO}^+$  cross section we observe is consistent with that observed previously by AB, as shown in Figure S1. AB found that this cross section declined as  $E^{-0.4}$  from 0.3 to 8 eV and then more rapidly as  $E^{-1.6}$  up to 50 eV. The resolution of these early ion beam experiments was insufficient to observe the more complicated energy dependence found here at lower energies, but the overall magnitude and qualitative shape are similar.

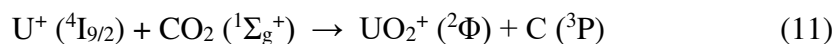
#### *UCO<sup>+</sup> product*

$\text{UCO}^+$  is a primary product in the reaction of  $\text{U}^+$  and  $\text{CO}_2$ , process 3. Equation 1 was used to model the product ion cross section, shown in Figure 4, and fitting parameters are detailed in Table 1. Analysis of the  $\text{UCO}^+$  cross section provides a threshold value of  $E_0(3) = 4.81 \pm 0.13 \text{ eV}$ . Using the relation  $D_0(\text{U}^+-\text{CO}) = D_0(\text{OC}=\text{O}) - E_0(3)$ ,  $D_0(\text{U}^+-\text{CO})$  is calculated to be  $0.71 \pm 0.13 \text{ eV}$ . This appears to be the first experimental measurement of the  $\text{U}^+-\text{CO}$  bond energy.

#### *UO<sub>2</sub><sup>+</sup> product*

$\text{UO}_2^+$  is formed by both the primary and secondary processes in the reaction of  $\text{U}^+$  and  $\text{CO}_2$ , reactions 4a and 4b. At higher energies, the primary reaction 4a is observed with a cross section that is comparable to the lower resolution study of AB. Using Equation 1, the analysis of the endothermic feature observed in the zero-pressure extrapolated data for the  $\text{UO}_2^+$  cross section provides a threshold energy of  $E_0(4a) = 3.97 \pm 0.12 \text{ eV}$ , shown in Figure 4. AB observed a similar threshold energy (although not explicitly stated) and commented that it appears to be well above the thermodynamic threshold, which is about 1 eV according to the literature. One possible explanation for this difference notes that the reaction of  $\text{U}^+ (^4\text{I}_{9/2}) + \text{CO}_2 (^1\Sigma_g^+)$  evolves along a

quartet spin surface. The ground state of  $\text{UO}_2^+$  is  $^2\Phi_u$  and the next three low-lying states are also doublet spin, whereas quartet spin states of  $\text{UO}_2^+$  ( $^4\text{H}_u$ ,  $^4\Sigma_u$ ,  $^4\Pi_u$ ) are calculated to lie 2.60 – 3.03 eV above the ground state.<sup>50</sup> These energies are consistent with the appearance of the  $\text{UO}_2^+$  product in reaction 4a although because the carbon atom product has triplet spin, reaction 4a = 11 is actually spin allowed.



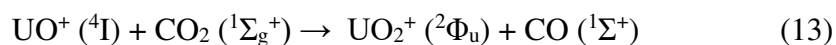
For the secondary reaction 4b, the overall reaction exothermicity is  $4.66 \pm 0.50$  eV. This is consistent with the low-energy (<0.5 eV) tail observed in this cross section, Figure 1, although the reaction is clearly very inefficient (0.02%). To get a better idea of the true energy dependence of the sequential reaction 4b, we note that the  $\text{UO}_2^+$  cross section is more appropriately envisioned by using the  $\text{UO}^+$  primary product as its precursor ion. This approach has proven effective for formation of the metal dioxide cations in the  $\text{Re}^+$ ,  $\text{Os}^+$ , and  $\text{Gd}^+$  reactions with  $\text{O}_2$  and  $\text{Gd}^+$  with  $\text{CO}_2$ .<sup>43, 51-53</sup> Figure 5 shows the reanalyzed  $\text{UO}_2^+$  cross section as a function of CM energy. When interpreted in this fashion, the  $\text{UO}_2^+$  cross sections for reaction 4b now have the same magnitudes at different  $\text{CO}_2$  pressures below 5 eV, and then diverge at higher energies where reaction 4a begins. Also shown in Figure 5 is a direct measurement of the cross section for reaction 12.



Direct comparison of these results is mediated by the fact that in the sequential reaction 4b, the  $\text{UO}^+$  “reactant” has a very different distribution of internal and kinetic energies than in the better controlled direct reaction. Nevertheless, the overall shapes of these cross sections are similar below the onset of reaction 4a but deviate in magnitude, a consequence of differing effective path lengths and the energy distributions.

The directly measured cross section for reaction 12 can also be compared to that of AB, as shown in Figure S2. Both the shapes (including the inefficient exothermic tail and large endothermic feature) and absolute magnitudes are comparable. For our data, the exothermic reaction cross section declines as  $E^{0.5}$  with a magnitude that is  $2.4 \pm 0.5\%$  of the collision cross section. AB noted that despite the exothermicity of reaction 12, the reaction displays an energetic

barrier of  $\sim 1.3$  eV. They hypothesized that this is related to the fact that dissociation of  $\text{CO}_2$  ( $^1\Sigma_g^+$ ) to  $\text{CO}$  ( $^1\Sigma^+$ ) does not lead to ground state  $\text{O}$  ( $^3\text{P}$ ) in a spin-allowed process but rather to excited state  $\text{O}$  ( $^1\text{D}$ ), 1.97 eV above the ground state. Similar to the discussion above, this observation may also be consistent with the reaction being spin-forbidden, reaction 13.



Thus, the endothermic feature may correspond to formation of quartet spin states of the  $\text{UO}_2^+$  product. Given an exothermicity of  $2.01 \pm 0.12$  eV, formation of the  $\text{UO}_2^+$  ( $^4\text{H}_u$ ,  $^4\Sigma_u$ ,  $^4\Pi_u$ ) states would be expected beginning at 0.6 – 1.0 eV. Consistent with this, analysis of this endothermic feature after accounting for the exothermic reactivity provides a threshold value of  $E_0$  (12) =  $0.64 \pm 0.14$  eV. Summed with a model for the exothermic reaction, this model can be seen to reproduce our experimental cross section well, as shown in Figure 5.

### Reaction of $\text{UO}^+ + \text{O}_2$

#### *UO<sub>2</sub><sup>+</sup> product*

$\text{UO}_2^+$  is formed in the exothermic, barrierless process 5 with high efficiency, as shown in Figure 2. By converting the cross section measured at the lowest energy (0.05 eV for four data sets) to a rate constant,  $k_5$ , we measure an average value of  $(6.4 \pm 1.9) \times 10^{-10}$  cm<sup>3</sup>/sec. Within experimental uncertainty, this matches the collision rate provided by the Langevin-Gioumoussis-Stevenson expression,  $k_{LGS}$ , for the  $\text{UO}^+ + \text{O}_2$  reaction of  $5.5 \times 10^{-10}$  cm<sup>3</sup>/s.

As the energy is increased further, the cross section declines as  $E^{-1/2}$ , in accord with the LGS collision cross section. At about 1 eV, the  $\text{UO}_2^+$  cross section begins to decrease more rapidly. This behavior can be attributed to angular momentum restrictions in the reaction moving from the entrance channel to the exit channel, as observed in other systems.<sup>54-55</sup> This occurs because the reduced mass of the  $\text{UO}_2^+ + \text{O}$  products is approximately one-half that of the  $\text{UO}^+ + \text{O}_2$  reactants. As a consequence, the centrifugal barrier in the product channel increases more rapidly than that in the reactant channel, eventually becoming larger such that the  $\text{UO}_3^+$  intermediates dissociate back to reactants, reducing the reaction efficiency. This behavior can be modeled using phase

This is the author's peer reviewed, accepted manuscript. However, the online version of record will be different from this version once it has been copyedited and typeset.

PLEASE CITE THIS ARTICLE AS DOI: 10.1063/5.0183836

space theory (PST)<sup>31</sup> in which angular momentum is explicitly conserved. The PST model assumes that the collision cross section is predicted by the LGS model (in agreement with the experiment at low energies) and requires knowledge of the polarizabilities of the neutral reactant and product, the rotational constants and vibrational frequencies of reactants and products, and the exothermicity for reaction 5 of  $2.45 \pm 0.12$  eV, calculated using  $D_0(\text{O}_2) = 5.115$  eV and  $D_0(\text{OU}^+\text{-O}) = 7.56 \pm 0.12$  eV. As shown in Figure 2b, the deviation in the experimental data from the LGS model (resulting from a return to reactants) is reproduced well by the PST calculated cross section. Notably, convoluting the LGS/PST model with the kinetic and internal energy distributions reproduces the data at very low energies nicely. If exothermicities of 2 or 3 eV are used instead, the PST model does not reproduce the observed behavior as well, providing additional evidence for the accuracy of the  $\text{UO}_2^+$  BDE determined here. In addition, the PST cross section calculated is smaller than the experimental cross section in the  $\sim 3 - 7$  eV energy range. This difference could be caused by evolution of the collision cross section to the hard sphere model at these elevated energies, or possibly to formation of an electronically excited  $\text{UO}_2^+$  product, neither of which are accounted for in the PST model.

At energies above about 5 eV, the  $\text{UO}_2^+$  cross section declines more rapidly. This behavior can be attributed to dissociation of the  $\text{UO}_2^+$  product to  $\text{UO}^+ + \text{O}$ , which can begin at  $D_0(\text{O}_2) = 5.115$  eV. The alternative dissociation to  $\text{U}^+ + \text{O}_2$  has a higher energy onset of  $8.01 \pm 0.13$  eV. This dissociation behavior is not included in the PST model shown.

#### *U<sup>+</sup> product*

$\text{U}^+$  is formed by CID of the  $\text{UO}^+$  precursor, process 6. Analysis of the endothermic cross section is shown in Figure 2a and provides a threshold value of  $E_0(6) = 8.05 \pm 0.14$  eV. This value agrees with previous measurements of the  $\text{U}^+\text{-O}$  bond dissociation energy, see below, as well as the recommended value of  $8.01 \pm 0.13$  eV.<sup>13</sup>

#### **Reaction of $\text{UO}^+ + \text{CO}$**

#### *U<sup>+</sup> product*

The bare uranium cation cross section provided by reaction of  $\text{UO}^+ + \text{CO}$  possesses two endothermic features. Similar features have been observed for several other metal oxide cation reactions with CO.<sup>43, 45-46, 56-58</sup> The low energy feature is attributed to process 9a, the reverse of reaction 2, and the feature at high energies corresponds to CID of  $\text{UO}^+$ , process 9b. Although the low-energy data is too noisy for a definitive analysis, we can use Equation 1 with the literature value for the endothermicity of reaction 9a,  $2.47 \pm 0.13$  eV, which is equivalent to the exothermicity of reaction 2. Figure 6 shows that this model reproduces the cross section behavior well. For the higher energy cross section feature, the threshold for the CID process is a direct measurement of the bond energy of  $\text{U}^+\text{-O}$ . Modeling with Equation 1 determines a threshold of  $E_0(9b) = 7.98 \pm 0.22$  eV, in excellent agreement with the  $\text{U}^+\text{-O}$  bond energy of  $8.01 \pm 0.13$  eV recommended by Zhang et al.<sup>13</sup> Figure 6 shows that the sum of the two models reproduces the original experimental cross section nicely throughout an extended energy range.

#### *UCO<sup>+</sup> product*

$\text{UCO}^+$  is formed in a primary reaction between  $\text{UO}^+$  and CO, process 8. Analysis of this cross section using Equation 1 (Figure 6) yields a threshold energy of  $E_0(8) = 7.46 \pm 0.19$  eV. Using the values obtained in this study with the relation  $D_0(\text{U}^+\text{-CO}) = D_0(\text{U}^+\text{-O}) - E_0(8)$ , a value of  $D_0(\text{U}^+\text{-CO}) = 0.52 \pm 0.29$  eV is obtained. This bond energy falls within experimental uncertainty of the analogous value obtained from the  $\text{U}^+ + \text{CO}_2$  reaction,  $0.71 \pm 0.13$  eV, such that the independent measurements of the  $\text{U}^+\text{-CO}$  bond energy obtained in this study are self-consistent. The falloff of the  $\text{UCO}^+$  product cross section after 10 eV is consistent with the thermodynamic threshold for  $\text{UCO}^+$  dissociation, which is equal to  $D_0(\text{CO}) = 11.1111 \pm 0.0003$  eV.<sup>35</sup>

#### *UO<sub>2</sub><sup>+</sup> product*

$\text{UO}_2^+$  is formed as a primary product in the reaction of  $\text{UO}^+$  and CO, process 7. Analysis of the  $\text{UO}_2^+$  cross section using Equation 1 provides a threshold energy of  $E_0(7) = 3.55 \pm 0.12$  eV (Figure 3). Using the bond energy of CO (11.11 and subtracting the  $E_0(7)$  value of 3.55 eV, we obtain an  $\text{OU}^+\text{-O}$  bond energy of  $7.56 \pm 0.12$  eV. This agrees well with previous literature values, see below.

### Comparison to Previous Thermochemical Measurements

Measurements of the  $U^+-O$  and  $OU^+-O$  bond energies provided by this study are  $7.98 \pm 0.22$  eV and  $8.05 \pm 0.14$  eV, and  $7.56 \pm 0.12$  eV, respectively. The bond energies obtained in this study are compared to the analogous previous measurements in Table 2. Our values are in reasonable agreement with those listed, falling within the uncertainties of the early direct measurements made by Armentrout and Beauchamp:  $D_0(U^+-O) = 8.0 \pm 0.3$  eV and  $D_0(OU^+-O) = 7.7 \pm 0.4$  eV.<sup>2</sup> Likewise, the present values lie within experimental uncertainty of the values recommended by Hildenbrand et al. based primarily on high-temperature mass spectrometry experiments:  $D_0(U^+-O) = 8.29 \pm 0.26$  eV and  $D_0(OU^+-O) = 7.97 \pm 0.58$  eV.<sup>59</sup> A later review of gas phase actinide chemistry by Lias et al. suggested values of  $D_0(U^+-O) = 8.33 \pm 0.23$  eV and  $D_0(OU^+-O) = 7.89 \pm 0.25$  eV.<sup>60</sup> The review by Marçalo and Gibson evaluated previous determinations of  $D_0(U^+-O)$  and  $D_0(OU^+-O)$  using Hess's law and refined the uncertainties associated with the values they classified as reliable.<sup>10</sup> They recommended  $D_{298}$  values that we correct (see introduction) to  $D_0(U^+-O) = 7.96 \pm 0.13$  eV and  $D_0(OU^+-O) = 7.63 \pm 0.15$  eV. Zhang et al.<sup>13</sup> measured  $D_0(U^+-O)$  to be  $7.88 \pm 0.09$  eV in their analysis of the reaction of  $U^+$  with CO and recommended a value of  $D_0(U^+-O) = 8.01 \pm 0.13$  eV taken from combining a recommended value for  $D_0(UO)$  and the precise IEs of U and UO. Again the present values lie well within the uncertainties of these values.

Using the relation  $D_0(AB) + IE(A) = IE(AB) + D_0(A^+-B)$  and the values computed by Zhang and Cheng at the CCSD(T) level of theory and the complete basis set extrapolation,<sup>12</sup> we obtain the theoretical values presented in Table 2. The theoretically obtained values  $D_0(U^+-O) = 8.01$  eV and  $D_0(OU^+-O) = 7.46$  eV agree quite well with the experimentally measured values  $D_0(U^+-O) = 7.98 \pm 0.22$  eV,  $8.05 \pm 0.14$  eV and  $D_0(OU^+-O) = 7.56 \pm 0.12$  eV obtained in the present study. The study of Zhang et al.<sup>13</sup> included a full Feller-Peterson-Dixon composite approach<sup>61-62</sup> and calculated a theoretical value for  $D_0(U^+-O)$  as 7.99 eV, which is also consistent with the experimentally measured BDE of  $UO^+$  presented here.

### Analysis of f orbital participation in bonding

The composition of the  $\text{UO}_2^+$  molecular orbitals (MOs) has previously been calculated by Ruipérez et al.<sup>50</sup> The valence MOs actively involved in the bonding of  $\text{UO}_2^+$  include  $1\pi_g$ ,  $2\pi_u$ ,  $3\sigma_g$ , and  $3\sigma_u$ , which contain four, four, two, and two electrons, respectively, along with a single unpaired electron in a nonbonding  $1\phi_u$  (pure 5f on U) MO. Their analysis shows that the  $1\pi_g$  and  $3\sigma_g$  MOs primarily utilize 6d orbitals on U, whereas the  $2\pi_u$  and  $3\sigma_u$  MOs have substantial 5f character. Our own natural bond orbital (NBO) analysis<sup>63</sup> (see supplementary material) shows that U has an effective charge of +2.67 e with each oxygen having -0.84 e. There are 0.88 e in 6d orbitals and 2.62 in 5f orbitals on uranium, such that nearly two 5f electrons are directly involved in the bonding.

Because  $\text{Sc}^+$ ,  $\text{Y}^+$ ,  $\text{La}^+$ , and  $\text{Gd}^+$  all have two valence electrons in non f orbitals and  $\text{Th}^+$  possesses similar bonding orbitals, comparisons between  $\text{U}^+$  and  $\text{Sc}^+$ ,  $\text{Y}^+$ ,  $\text{La}^+$ ,  $\text{Gd}^+$ , and  $\text{Th}^+$  have been useful in our previous analyses of  $\text{UH}^+$  and  $\text{UO}^+$ .<sup>13,26</sup> The  $\text{OM}^+\text{-O}$  BDEs for these species are  $D_0(\text{OSc}^+\text{-O}) = 1.72 \pm 0.19$  eV,<sup>64</sup>  $D_0(\text{OY}^+\text{-O}) = 1.76 \pm 0.16$  eV,<sup>64</sup>  $D_0(\text{OLa}^+\text{-O}) = 0.99 \pm 0.31$  eV,<sup>64</sup>  $D_0(\text{OGd}^+\text{-O}) = 2.86 \pm 0.08$  eV,<sup>53</sup> and  $D_0(\text{OTh}^+\text{-O}) = 4.94 \pm 0.06$  eV.<sup>65</sup> Previously, we pointed out that the larger BDE for  $\text{Th}^+$  could be explained by the fact that the transition metals have no accessible f electrons. There, the  $2\pi_u$  and  $3\sigma_u$  MOs are completely nonbonding, such that they distort leading to bent structures for these dioxides. Because the 5f electrons can participate for Th, the molecule is linear<sup>66-67</sup> and the second oxide BDE is enhanced.<sup>65</sup> In the case of  $\text{ThO}_2^+$ , the valence electron configuration is  $(1\pi_g)^4(2\pi_u)^4(3\sigma_g)^2(3\sigma_u)^1$ . When we compare the second oxide bond of thorium with that of uranium,  $D_0(\text{OU}^+\text{-O}) = 7.56 \pm 0.12$  eV, we see an even larger enhancement compared to the transition metal dioxide cations. Note that this is a result of adding two electrons, one to the bonding  $3\sigma_u$  MO and one to the nonbonding  $1\phi_u$  MO, such that the valence electron configuration of  $\text{UO}_2^+$  is  $(1\pi_g)^4(2\pi_u)^4(3\sigma_g)^2(3\sigma_u)^2(1\phi_u)^1$ . Clearly, the addition of a single electron to the six bonding MOs would not be expected to increase the bond energy by the amount observed. Therefore, we attribute this strong increase to a higher degree of participation by the 5f orbitals in the bonding of  $\text{UO}_2^+$  compared to  $\text{ThO}_2^+$ . Indeed, comparison of the NBO analysis of

these two molecules indicates similar amounts of 6d participation, 0.88 e and 0.75 e, respectively, but much larger 5f orbital participation, 1.62 e on U (excluding the nonbonding  $\phi$  electron) versus 0.58 e on Th. This enhanced 5f orbital participation enables the second oxide bond to nearly equal (94%) the first oxide bond,  $D_0(\text{U}^+-\text{O}) = 8.01 \pm 0.13 \text{ eV}$ .<sup>13</sup>

Su et al. provided a Cl K-edge X-ray absorption spectroscopy and relative density functional theory study that quantified the participation of f-orbitals in actinide bonding for  $\text{AnCl}_6^{2-}$  (An = Th, U, Np, Pu).<sup>68</sup> For Th, the 6d and 5f orbitals are similar in energy, and, as a result, are intermixed. For U, there is a clear separation between the energies of the 6d and 5f orbitals, with the highest energy 5f orbital calculated to lie  $\sim 0.25 \text{ eV}$  lower in energy than the lowest energy 6d orbital. This energy separation between 6d and 5f orbitals becomes more pronounced for Np and Pu with energy differences between the 6d and 5f orbitals being  $\sim 1$  and  $\sim 1.5 \text{ eV}$ , respectively. A result of the progressive lowering of the energies of the 5f orbitals across the actinide series is the increased participation of f orbitals in actinide bonding. Here, we quantify that this enhanced 5f orbital participation leads to a substantial increase in the thermodynamic stability of  $\text{UO}_2^+$  relative to  $\text{ThO}_2^+$  and especially transition metal dioxide cations.

### Supplementary Material

See supplementary material for the output of the NBO analyses of  $\text{UO}_2^+$  and  $\text{ThO}_2^+$ .

### Acknowledgement

This work is supported by the Heavy Element Chemistry Program, Office of Basic Energy Sciences, U.S. Department of Energy through Grant DE\_SC0012249.

### Author Declarations

The authors have no conflicts to disclose.

## REFERENCES

1. Armentrout, P. B.; Beauchamp, J. L., Reactions of  $U^+$  and  $UO^+$  with  $O_2$ ,  $CO$ ,  $CO_2$ ,  $COS$ ,  $CS_2$  and  $D_2O$ . *Chem. Phys.* **1980**, *50*, 27-36.
2. Armentrout, P. B.; Beauchamp, J. L., Collision Induced Dissociation of  $UO^+$  and  $UO_2^+$ . *Chem. Phys.* **1980**, *50*, 21-25.
3. Hunt, R. D.; Andrews, L., Reactions of pulsed-laser evaporated uranium atoms with molecular oxygen: Infrared spectra of  $UO$ ,  $UO_2$ ,  $UO_3$ ,  $UO_2^+$ ,  $UO_2^{2+}$ , and  $UO_3-O_2$  in solid argon. *J. Chem. Phys.* **1993**, *98* (5), 3690-3696.
4. Zhou, M.; Andrews, L.; Ismail, N.; Marsden, C., Infrared spectra of  $UO_2$ ,  $UO_2^+$ , and  $UO_2^-$  in solid neon. *J. Phys. Chem. A* **2000**, *104* (23), 5495-5502.
5. Majumdar, D.; Balasubramanian, K.; Nitsche, H., A comparative theoretical study of bonding in  $UO_2^{++}$ ,  $UO_2^+$ ,  $UO_2$ ,  $UO_2^-$ ,  $OUCO$ ,  $O_2U(CO)_2$  and  $UO_2CO_3$ . *Chem. Phys. Lett.* **2002**, *361* (1-2), 143-151.
6. Han, J.; Goncharov, V.; Kaledin, L. A.; Komissarov, A. V.; Heaven, M. C., Electronic spectroscopy and ionization potential of  $UO_2$  in the gas phase. *J. Chem. Phys.* **2004**, *120* (11), 5155-5163.
7. Gagliardi, L.; Heaven, M. C.; Krogh, J. W.; Roos, B. O., The electronic spectrum of the  $UO_2$  molecule. *J. Am. Chem. Soc.* **2005**, *127* (1), 86-91.
8. Goncharov, V.; Kaledin, L. A.; Heaven, M. C., Probing the electronic structure of  $UO^+$  with high-resolution photoelectron spectroscopy. *J. Chem. Phys.* **2006**, *125* (13), 133202.
9. Merritt, J. M.; Han, J.; Heaven, M. C., Spectroscopy of the  $UO_2^+$  cation and the delayed ionization of  $UO_2$ . *J. Chem. Phys.* **2008**, *128* (8), 084304.
10. Marçalo, J.; Gibson, J. K., Gas-Phase Energetics of Actinide Oxides: An Assessment of Neutral and Cationic Monoxides and Dioxides from Thorium to Curium. *J. Phys. Chem. A* **2009**, *113* (45), 12599-12606.
11. Kovács, A.; Pogány, P.; Konings, R. J. M., Theoretical Study of Bond Distances and Dissociation Energies of Actinide Oxides  $AnO$  and  $AnO_2$ . *Inorg. Chem.* **2012**, *51* (8), 4841-4849.
12. Zhang, C.; Cheng, L., Route to Chemical Accuracy for Computational Uranium Thermochemistry. *J. Chem. Theory Comput.* **2022**, *18* (11), 6732-6741.
13. Zhang, W.; Hunt, A. R. E.; Kim, J. S.; Demireva, M.; Peterson, K. A.; Armentrout, P. B., Bond Energies of  $UO^+$  and  $UC^+$ : Guided Ion Beam and Quantum Chemical Studies of the Reactions of Uranium Cation with  $O_2$  and  $CO$ . *Isr. J. Chem.* **2023**, *63* (7-8), e202300026.
14. Pedley, J. B.; Marshall, E. M., Thermochemical Data for Gaseous Monoxides. *J. Phys. Chem. Ref. Data* **1983**, *12* (4), 967-1031.
15. Konings, R. J. M.; Benes, O.; Kovacs, A.; Manara, D.; Sedmidubsky, D.; Gorokhov, L.; Iorish, V. S.; Yungman, V.; Shenyavskaya, E.; Osina, E., The Thermodynamic Properties of the f-Elements and their Compounds. Part 2. The Lanthanide and Actinide Oxides. *J. Phys. Chem. Ref. Data* **2014**, *43*, 013101.
16. Loh, S. K.; Hales, D. A.; Lian, L.; Armentrout, P. B., Collision-Induced Dissociation of  $Fe_n^+$  ( $n = 2 - 10$ ) with Xe: Ionic and Neutral Iron Cluster Binding Energies. *J. Chem. Phys.* **1989**, *90*, 5466-5485.
17. Schultz, R. H.; Armentrout, P. B., Reactions of  $N_4^+$  with Rare Gases from Thermal to 10 eV c.m.: Collision-Induced Dissociation, Charge Transfer, and Ligand Exchange. *Int. J. Mass Spectrom. Ion Processes* **1991**, *107*, 29-48.
18. Sievers, M. R.; Chen, Y.-M.; Elkind, J. L.; Armentrout, P. B., Reactions of  $Y^+$ ,  $Zr^+$ ,  $Nb^+$ , and  $Mo^+$  with  $H_2$ ,  $HD$ , and  $D_2$ . *J. Phys. Chem.* **1996**, *100*, 54-62.
19. Haynes, C. L.; Armentrout, P. B., Thermochemistry and Structures of  $CoC_3H_6^+$ : Metallacycle and Metal-Alkene Isomers. *Organomet.* **1994**, *13*, 3480-3490.
20. Kickel, B. L.; Armentrout, P. B., Reactions of  $Fe^+$ ,  $Co^+$  and  $Ni^+$  with Silane. Electronic State Effects, Comparison to Reactions with Methane, and  $M^+-SiH_x$  ( $x = 0 - 3$ ) Bond Energies. *J. Am. Chem. Soc.* **1995**, *117*, 764-773.

21. Kickel, B. L.; Armentrout, P. B., Guided Ion Beam Studies of the Reactions of  $\text{Mn}^+$ ,  $\text{Cu}^+$ , and  $\text{Zn}^+$  with Silane.  $\text{M}^+-\text{SiH}_x$  ( $x = 0 - 3$ ) Bond Energies. *J. Phys. Chem* **1995**, *99*, 2024-2032.
22. Clemmer, D. E.; Chen, Y.-M.; Khan, F. A.; Armentrout, P. B., State-Specific Reactions of  $\text{Fe}^+(\text{a}^6\text{D}, \text{a}^4\text{F})$  with  $\text{D}_2\text{O}$  and Reactions of  $\text{FeO}^+$  with  $\text{D}_2$ . *J. Phys. Chem.* **1994**, *98*, 6522-6529.
23. Kickel, B. L.; Armentrout, P. B., Guided Ion Beam Studies of the Reactions of Group 3 Metal Ions ( $\text{Sc}^+$ ,  $\text{Y}^+$ ,  $\text{La}^+$ , and  $\text{Lu}^+$ ) with Silane. Electronic State Effects, Comparison to Reactions with Methane, and  $\text{M}^+-\text{SiH}_x$  ( $x = 0 - 3$ ) Bond Energies. *J. Am. Chem. Soc.* **1995**, *117*, 4057-4070.
24. Sansonetti, J. E.; Martin, W. C., Handbook of Basic Atomic Spectroscopic Data. *J. Phys. Chem. Ref. Data* **2005**, *34* (4), 1559-2259.
25. Blaise, J.; Wyart, J.-F., *Energy Levels and Atomic Spectra of Actinides*. Paris, 1992.
26. Zhang, W.-J.; Demireva, M.; Kim, J.; de Jong, W. A.; Armentrout, P. B., Reactions of  $\text{U}^+$  with  $\text{H}_2$ ,  $\text{D}_2$ , and  $\text{HD}$  Studied by Guided Ion Beam Tandem Mass Spectrometry and Theory. *J. Phys. Chem. A* **2021**, *125* (36), 7825-7839.
27. Hales, D. A.; Lian, L.; Armentrout, P. B., Collision-Induced Dissociation of  $\text{Nb}_n^+$  ( $n = 2 - 11$ ): Bond Energies and Dissociation Pathways. *Int. J. Mass Spectrom. Ion Processes* **1990**, *102*, 269-301.
28. Daly, N. R., Scintillation Type Mass Spectrometer Ion Detector. *Rev. Sci. Instrum.* **1960**, *31*, 264-267.
29. Ervin, K. M.; Armentrout, P. B., Translational Energy Dependence of  $\text{Ar}^+ + \text{XY} \rightarrow \text{ArX}^+ + \text{Y}$  ( $\text{XY} = \text{H}_2, \text{D}_2, \text{HD}$ ) from Thermal to 30 eV c.m. *J. Chem. Phys.* **1985**, *83* (1), 166-189.
30. Armentrout, P. B., The Kinetic Energy Dependence of Ion-Molecule Reactions: Guided Ion Beams and Threshold Measurements. *Int. J. Mass Spectrom.* **2000**, *200*, 219-241.
31. Chesnavich, W. J.; Bowers, M. T., Theory of translationally driven reactions. *J. Phys. Chem.* **1979**, *83* (8), 900-905.
32. Muntean, F.; Armentrout, P. B., Guided Ion Beam Study of Collision-Induced Dissociation Dynamics: Integral and Differential Cross Sections. *J. Chem. Phys.* **2001**, *115*, 1213-1228.
33. Armentrout, P. B., The Power of Accurate Energetics (or Thermochemistry: What is it Good for?). *J. Am. Soc. Mass Spectrom.* **2013**, *24*, 173-185.
34. Weber, M. E.; Elkind, J. L.; Armentrout, P. B., Kinetic Energy Dependence of  $\text{Al}^+ + \text{O}_2 \rightarrow \text{AlO}^+ + \text{O}$ . *J. Chem. Phys.* **1986**, *84*, 1521-1529.
35. Ruscic, B.; Bross, D. H. Active Thermochemical Tables (ATcT) values based on ver. 1.122g of the Thermochemical Network. available at ATcT.anl.gov (accessed 4/29/20).
36. Langevin, P., Une Formule Fondamentale de Theorie Cinetique. *Ann. Chim. Phys. Ser. 8* **1905**, *5*, 245-288.
37. Gioumoussis, G.; Stevenson, D. P., Reactions of Gaseous Molecule Ions with Gaseous Molecules. V. Theory. *J. Chem. Phys.* **1958**, *29*, 294-299.
38. Heller, E. J.; Brown, R. C., Radiationless Transitions in a New Light. *J. Chem. Phys.* **1983**, *79*, 3336-3351.
39. Lorquet, J. C.; Leyh-Nihant, B., Nonadiabatic unimolecular reactions. 1. A statistical formulation for the rate constants. *J. Phys. Chem.* **1988**, *92*, 4778-4783.
40. Dressler, R. A.; Arnold, S. T.; Murad, E., Charge-transfer Dynamics in Ion-polyatomic Molecule Collisions:  $\text{X}^+ + \text{H}_2\text{O}$  ( $\text{X} = \text{N}, \text{Kr}$ ) Luminescence Study. *J. Chem. Phys.* **1995**, *103*, 9989-10000.
41. Rue, C.; Armentrout, P. B.; Kretzschmar, I.; Schröder, D.; Harvey, J. N.; Schwarz, H., Kinetic-energy Dependence of Competitive Spin-allowed and Spin-forbidden Reactions:  $\text{V}^+ + \text{CS}_2$ . *J. Chem. Phys.* **1999**, *110* (16), 7858-7870.
42. Demireva, M.; Kim, J.; Armentrout, P. B., Gadolinium (Gd) Oxide, Carbide, and Carbonyl Cation Bond Energies and Evaluation of the  $\text{Gd} + \text{O} \rightarrow \text{GdO}^+ + \text{e}^-$  Chemi-Ionization Reaction Enthalpy. *J. Phys. Chem. A* **2016**, *120*, 8550-8563.
43. Demireva, M.; Armentrout, P. B., Activation of  $\text{CO}_2$  by Gadolinium Cation ( $\text{Gd}^+$ ): Energetics and Mechanism from Experiment and Theory. *Top. Catal.* **2018**, *61*, 3-19.

44. Armentrout, P. B.; Cox, R. M.; Sweeny, B. C.; Ard, S. G.; Shuman, N. S.; Viggiano, A. A., Lanthanides as Catalysts: Guided Ion Beam and Theoretical Studies of  $\text{Sm}^+ + \text{COS}$ . *J. Phys. Chem. A* **2018**, *122* (3), 737-749.
45. Ghiassaei, M.; Kim, J.; Armentrout, P. B., Evaluation of the Exothermicity of the Chemi-ionization Reaction  $\text{Nd} + \text{O} \rightarrow \text{NdO}^+ + \text{e}^-$  and Neodymium Oxide, Carbide, Dioxide, and Carbonyl Cation Bond Energies. *J. Chem. Phys.* **2019**, *150*, 144309.
46. Ghiassaei, M.; Stevenson, B. C.; Armentrout, P. B., Evaluation of the  $\text{Pr} + \text{O} \rightarrow \text{PrO}^+ + \text{e}^-$  Chemi-ionization Reaction Enthalpy and Praseodymium Oxide, Carbide, Dioxide, and Carbonyl Cation Bond Energies. *Phys. Chem. Chem. Phys.* **2021**, *23*, 2938-2952.
47. Johnson III, R. D. NIST Computational Chemistry Comparison and Benchmark Database. <http://cccbdb.nist.gov/> (accessed Nov. 11, 2022).
48. Wilson, R. G.; Brewer, G. R., *Ion Beams with Applications to Ion Implantation*. Wiley: New York, 1973.
49. Bubas, A.; Owen, C.; Armentrout, P., Reactions of atomic thorium and uranium cations with  $\text{CF}_4$  studied by guided ion beam tandem mass spectrometry. *International Journal of Mass Spectrometry* **2021**, *472*, 116778.
50. Ruipérez, F.; Danilo, C.; Réal, F.; Flament, J.-P.; Vallet, V.; Wahlgren, U., An ab Initio Theoretical Study of the Electronic Structure of  $\text{UO}_2^+$  and  $[\text{UO}_2(\text{CO}_3)_3]^{5-}$ . *J. Phys. Chem. A* **2009**, *113* (8), 1420-1428.
51. Armentrout, P. B., The Bond Energy of  $\text{ReO}^+$ : Guided Ion-Beam and Theoretical Studies of the Reaction of  $\text{Re}^+ (^7\text{S})$  with  $\text{O}_2$ . *J. Chem. Phys.* **2013**, *139*, 084305.
52. Hinton, C. S.; Citir, M.; Armentrout, P. B., Guided Ion-Beam and Theoretical Studies of the Reaction of  $\text{Os}^+ (^6\text{D})$  with  $\text{O}_2$ : Adiabatic and Nonadiabatic Behavior. *Int. J. Mass Spectrom.* **2013**, *354-355*, 87-98.
53. Demireva, M.; Armentrout, P. B., Gadolinium Cation ( $\text{Gd}^+$ ) Reaction with  $\text{O}_2$ : Potential Energy Surface Mapped Experimentally and with Theory. *J. Chem. Phys.* **2017**, *146*, 174302.
54. Burley, J. D.; Ervin, K. M.; Armentrout, P. B., Translational Energy Dependence of  $\text{O}^+(^4\text{S}) + \text{H}_2(\text{D}_2, \text{HD}) \rightarrow \text{OH}^+(\text{OD}^+) + \text{H}(\text{D})$  from Thermal to 30 eV c.m. *Int. J. Mass Spectrom. Ion Processes* **1987**, *80*, 153-175.
55. Fisher, E. R.; Elkind, J. L.; Clemmer, D. E.; Georgiadis, R.; Loh, S. K.; Aristov, N.; Sunderlin, L. S.; Armentrout, P. B., Reactions of Fourth Period Metal Ions ( $\text{Ca}^+ - \text{Zn}^+$ ) with  $\text{O}_2$ : Metal Oxide Ion Bond Energies. *J. Chem. Phys.* **1990**, *93*, 2676-2691.
56. Armentrout, P. B.; Cox, R. M., Potential Energy Surface for Reaction of  $\text{Sm}^+ + \text{CO}_2 \rightarrow \text{SmO}^+ + \text{CO}$ : Guided Ion Beam and Theoretical Studies. *Phys. Chem. Chem. Phys.* **2017**, *19*, 11075-11088.
57. Owen, C. J.; Kim, J.; Armentrout, P. B., Holmium (Ho) Oxide, Carbide, and Dioxide Cation Bond Energies and Evaluation of the  $\text{Ho} + \text{O} \rightarrow \text{HoO}^+ + \text{e}^-$  Chemi-ionization Reaction Enthalpy. *J. Chem. Phys.* **2021**, *155* (9), 094303.
58. Ghiassaei, M.; Christensen, E. G.; Armentrout, P. B., Evaluation of the  $\text{Dy} + \text{O} \rightarrow \text{DyO}^+ + \text{e}^-$  Chemi-ionization Reaction Exothermicity and Dysprosium Oxide, Carbide, Dioxide, and Sulfoxides Cation Bond Energies. *J. Phys. Chem. A* **2023**, *127*, 169-180.
59. Hildenbrand, D. L.; Gurvich, L. V.; Yungman, V. S. *The Chemical Thermodynamics of Actinide Elements and Compounds. Part 13: The Gaseous Actinide Ions*; IAEA: Vienna, 1985.
60. Lias, S. G.; Bartmess, J. E.; Liebman, J. F.; Holmes, J. L.; Levin, R. D.; Mallard, W. G., Gas-Phase Ion and Neutral Thermochemistry. *J. Phys. Chem. Ref. Data Suppl. 1* **1988**, *17*, 1.
61. Feller, D.; Peterson, K. A.; Dixon, D. A., A Survey of Factors Contributing to Accurate Theoretical Predictions of Atomization Energies and Molecular Structures. *J. Chem. Phys.* **2008**, *129* (20), 204105.
62. Vasiliu, M.; Peterson, K. A.; Gibson, J. K.; Dixon, D. A., Reliable Potential Energy Surfaces for the Reactions of  $\text{H}_2\text{O}$  with  $\text{ThO}_2$ ,  $\text{PaO}_2^+$ ,  $\text{UO}_2^{2+}$ , and  $\text{UO}_2^+$ . *J. Phys. Chem. A* **2015**, *119* (46), 11422-11431.
63. Glendening, E. D.; Reed, A. E.; Carpenter, J. E.; Weinhold, F. *NBO Version 3.1*, Gaussian Inc.: Pittsburgh, 2003.

This is the author's peer reviewed, accepted manuscript. However, the online version of record will be different from this version once it has been copyedited and typeset.

PLEASE CITE THIS ARTICLE AS DOI: 10.1063/5.0183836

64. Clemmer, D. E.; Dalleska, N. F.; Armentrout, P. B., Gas Phase Thermochemistry of the Group 3 Dioxides: ScO<sub>2</sub>, YO<sub>2</sub> and LaO<sub>2</sub>. *Chem. Phys. Lett.* **1992**, *190*, 259-265.
65. Armentrout, P. B.; Peterson, K. A., Guided Ion Beam and Quantum Chemical Investigation of the Thermochemistry of Thorium Dioxide Cations: Thermodynamic Evidence for Participation of *f* Orbitals in Bonding. *Inorg. Chem.* **2020**, *59* (5), 3118-3131.
66. Wadt, W. R., Why UO<sub>2</sub><sup>2+</sup> is Linear and Isoelectronic ThO<sub>2</sub> is Bent. *J. Am. Chem. Soc.* **1981**, *103*, 6053-6057.
67. Dyllal, K. G., Bonding and bending in the actinyls. *Molec. Phys.* **1999**, *96* (4), 511-518.
68. Su, J.; Batista, E. R.; Boland, K. S.; Bone, S. E.; Bradley, J. A.; Cary, S. K.; Clark, D. L.; Conradson, S. D.; Ditter, A. S.; Kaltsoyannis, N., Energy-degeneracy-driven covalency in actinide bonding. *J. Am. Chem. Soc.* **2018**, *140* (51), 17977-17984.

Table 1. Fitting parameters from Equation 1 for the indicated reaction.

	Reaction	$\sigma_0$ ( $\text{\AA}^2 \text{eV}^{1-n}$ )	$E_0$ (eV)	n	p	$E_D$ (eV)	$D(\text{U}^+-\text{L})$ (eV)
3	$\text{U}^+ + \text{CO}_2 \rightarrow \text{UCO}^+ + \text{O}$	$0.09 \pm 0.03$	$4.81 \pm 0.13$	$1.8 \pm 0.3$	3	6.4	$0.71 \pm 0.13$
4a	$\text{U}^+ + \text{CO}_2 \rightarrow \text{UO}_2^+ + \text{C}$	$0.14 \pm 0.04$	$3.97 \pm 0.12$	$2.6 \pm 0.2$			
6	$\text{UO}^+ + \text{O}_2 \rightarrow \text{U}^+ + \text{O} + \text{O}_2$	$0.02 \pm 0.01$	$8.05 \pm 0.14$	$1.9 \pm 0.1$			$8.05 \pm 0.14$
7	$\text{UO}^+ + \text{CO} \rightarrow \text{UO}_2^+ + \text{C}$	$0.24 \pm 0.07$	$3.55 \pm 0.12$	$2.3 \pm 0.2$	3	10.3	$7.56 \pm 0.12$
8	$\text{UO}^+ + \text{CO} \rightarrow \text{UCO}^+ + \text{O}$	$0.069 \pm 0.021$	$7.46 \pm 0.19$	$1.9 \pm 0.2$	3	10.7	$0.52 \pm 0.29$
9a	$\text{UO}^+ + \text{CO} \rightarrow \text{U}^+ + \text{CO}_2$	$(4.1 \pm 0.5) \times 10^{-3}$	$2.47 \pm 0.13$	$1.1 \pm 0.1$	3	8.0	$7.98 \pm 0.13$
9b	$\text{UO}^+ + \text{CO} \rightarrow \text{U}^+ + \text{O} + \text{CO}$	$0.045 \pm 0.008$	$7.98 \pm 0.22$	$1.3 \pm 0.1$	2	14.8	$7.98 \pm 0.22$
13	$\text{UO}^+ + \text{CO}_2 \rightarrow \text{UO}_2^+ + \text{CO}$	$0.61 \pm 0.11$	$0.64 \pm 0.14$	$2.1 \pm 0.1$	4	7.2	

Table 2. Comparison of experimental and theoretical values of  $D_0(U^+-L)$  (eV).

Species	This Work	Literature (Experiment)	Literature (Theory)
U <sup>+</sup> -O	7.98 ± 0.22	8.0 ± 0.3 <sup>a</sup>	7.99 <sup>e</sup>
	8.05 ± 0.14	8.29 ± 0.26 <sup>b</sup>	8.01 <sup>f</sup>
		8.33 ± 0.23 <sup>c</sup>	
		7.96 ± 0.13 <sup>d</sup>	
		7.88 ± 0.09 <sup>e</sup>	
		8.01 ± 0.13 <sup>e*</sup>	
OU <sup>+</sup> -O	7.56 ± 0.12	7.7 ± 0.4 <sup>a</sup>	7.46 <sup>f</sup>
		7.97 ± 0.58 <sup>b</sup>	
		7.89 ± 0.25 <sup>c</sup>	
		7.63 ± 0.15 <sup>d</sup>	
U <sup>+</sup> -CO	0.71 ± 0.13		
	0.52 ± 0.29		

<sup>a</sup>Reference <sup>2</sup>. <sup>b</sup>Reference <sup>59</sup> corrected to 0 K. <sup>c</sup>Reference <sup>60</sup> corrected to 0 K. <sup>d</sup>Recommended value from Reference <sup>10</sup> corrected to 0 K. <sup>e</sup>Reference <sup>13</sup>. <sup>e\*</sup>Recommended value from ref. <sup>13</sup>.

<sup>f</sup>Derived using the relation  $D_0(AB) + IE(A) = IE(AB) + D_0(A^+-B)$  and CCSD(T)/CBS values from Reference <sup>12</sup>.

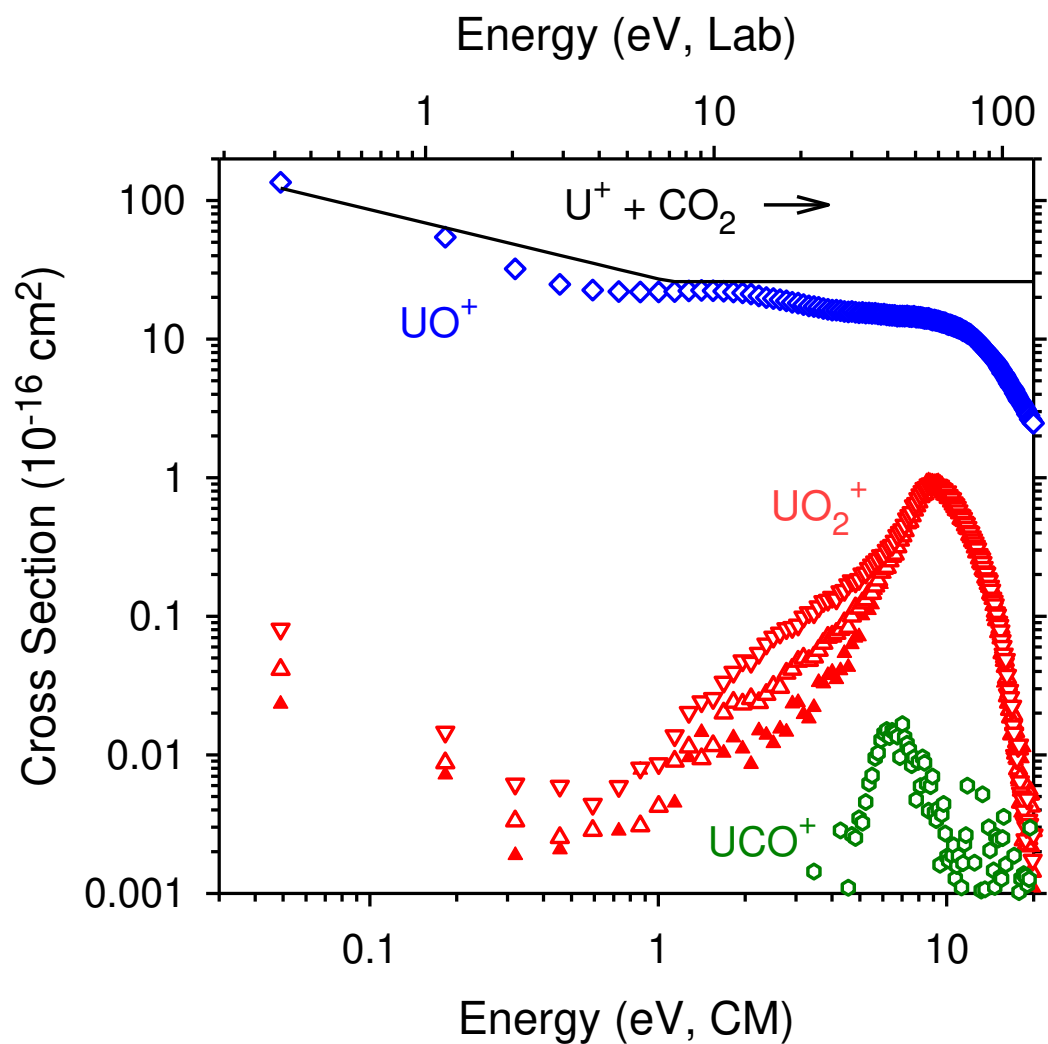


Figure 1. Product ion cross sections for the reaction of  $U^+ + CO_2$  as a function of ion kinetic energy in the center-of-mass (lower x-axis) and laboratory (upper x-axis) frames. The solid black line represents the Langevin-Gioumouisis-Stevenson (LGS) cross section at low energies and half the hard-sphere (HS) cross section at higher energies. The pressure-dependent cross section of  $UO_2^+$  is shown by the inverted red triangles (0.4 mTorr), upright red triangles (0.2 mTorr), and upright red filled triangles (0.1 mTorr). Pressure independent cross sections for the  $UO^+$  and  $UCO^+$  products are represented by blue diamonds and green hexagons, respectively.

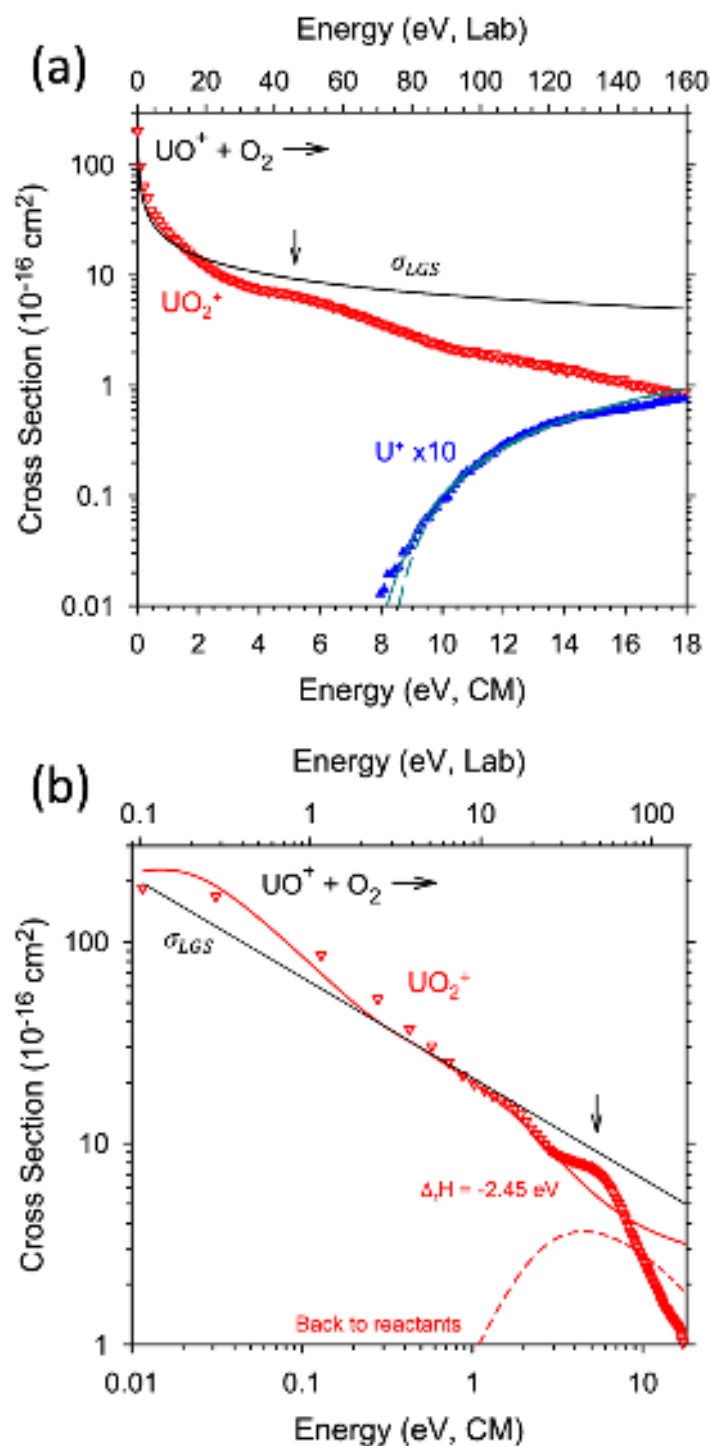


Figure 2. (a) Product ion cross sections for the reaction of  $\text{UO}^+ + \text{O}_2$  as a function of ion kinetic energy in the center-of-mass (lower x-axis) and laboratory (upper x-axis) frames. The solid black line represents the Langevin-Gioumoussis-Stevenson (LGS) cross section. Pressure independent cross sections for  $\text{UO}_2^+$  and  $\text{U}^+$  products are shown by the inverted red triangles and upright blue filled triangles, respectively. The model of the CID reaction using Eq. 1 is shown convoluted over the reactant internal and kinetic energies (cyan solid line) and unconvoluted (cyan dashed line). The arrow marks  $D_0(\text{O}_2) = 5.115 \text{ eV}$ . (b) Experimental  $\text{UO}_2^+$  cross section (inverted red triangles) compared to the LGS cross

section (black line) and Phase Space Theory (PST) calculated cross section convoluted over the reactant internal and kinetic energies for an exothermicity of  $2.45 \text{ eV}$  (solid red line). The dashed red line is the PST calculated cross section for returning to the  $\text{UO}^+$  and  $\text{O}_2$  reactants. Above  $1 \text{ eV}$ , the sum of the solid and dashed red lines reproduces  $\sigma_{\text{LGS}}$ .

This is the author's peer reviewed, accepted manuscript. However, the online version of record will be different from this version once it has been copyedited and typeset.  
PLEASE CITE THIS ARTICLE AS DOI: 10.1063/5.0183836

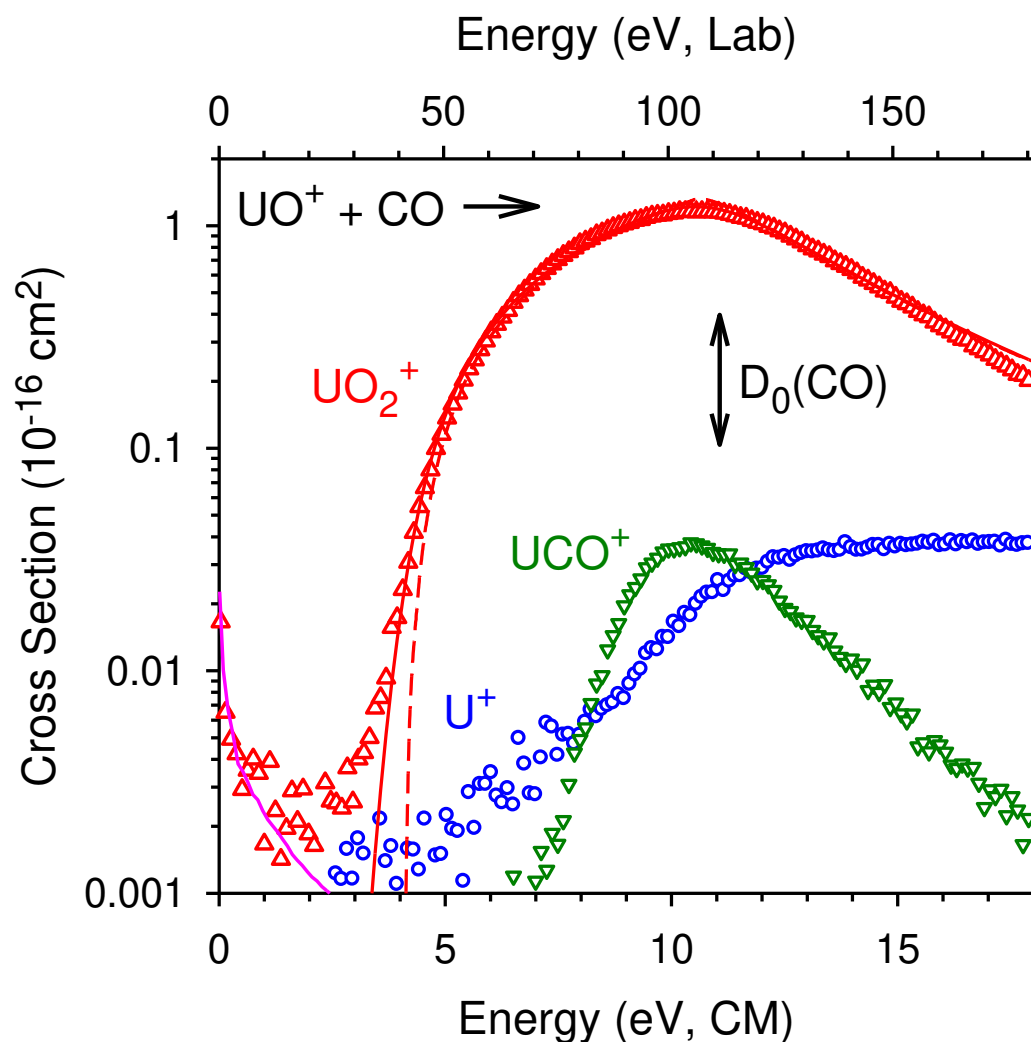


Figure 3. Product ion cross sections for the reaction of  $\text{UO}^+ + \text{CO}$  as a function of ion kinetic energy in the center-of-mass (lower x-axis) and laboratory (upper x-axis) frames. Symbols show cross sections for  $\text{UO}_2^+$  (red triangles),  $\text{U}^+$  (blue circles), and  $\text{UCO}^+$  (green inverted triangles). The model of the  $\text{UO}_2^+$  product using Eq. 1 is shown convoluted over the reactant internal and kinetic energies (solid line) and unconvoluted (dashed line). The solid pink line is the  $\text{UO}_2^+$  cross section from the reaction of  $\text{UO}^+ + \text{O}_2$  (shown in Figure 2) scaled down by a factor of  $10^4$ . The vertical arrow shows  $D_0(\text{CO}) = 11.11$  eV.

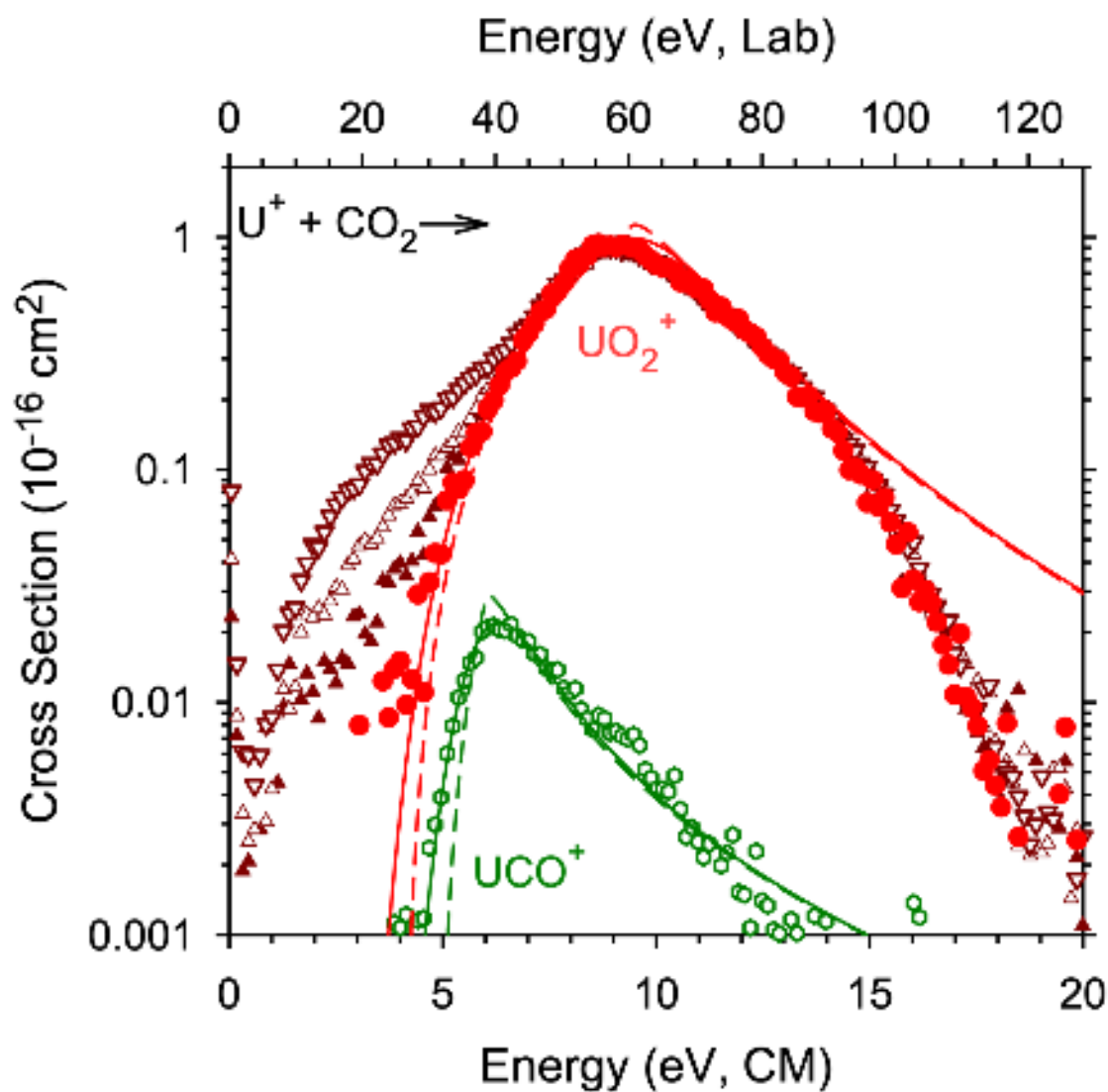


Figure 4. Product ion cross sections for the reaction of  $\text{U}^+ + \text{CO}_2$  as a function of ion kinetic energy in the center-of-mass (lower x-axis) and laboratory (upper x-axis) frames. The pressure-dependent cross sections of  $\text{UO}_2^+$  from Figure 1 are shown by the brick red triangles and the zero-pressure extrapolated cross section is shown by red circles. The  $\text{UCO}^+$  cross section is shown by the green hexagons. The models of both reactions using Eq. 1 are shown convoluted over the reactant internal and kinetic energies (solid lines) and unconvoluted (dashed lines).

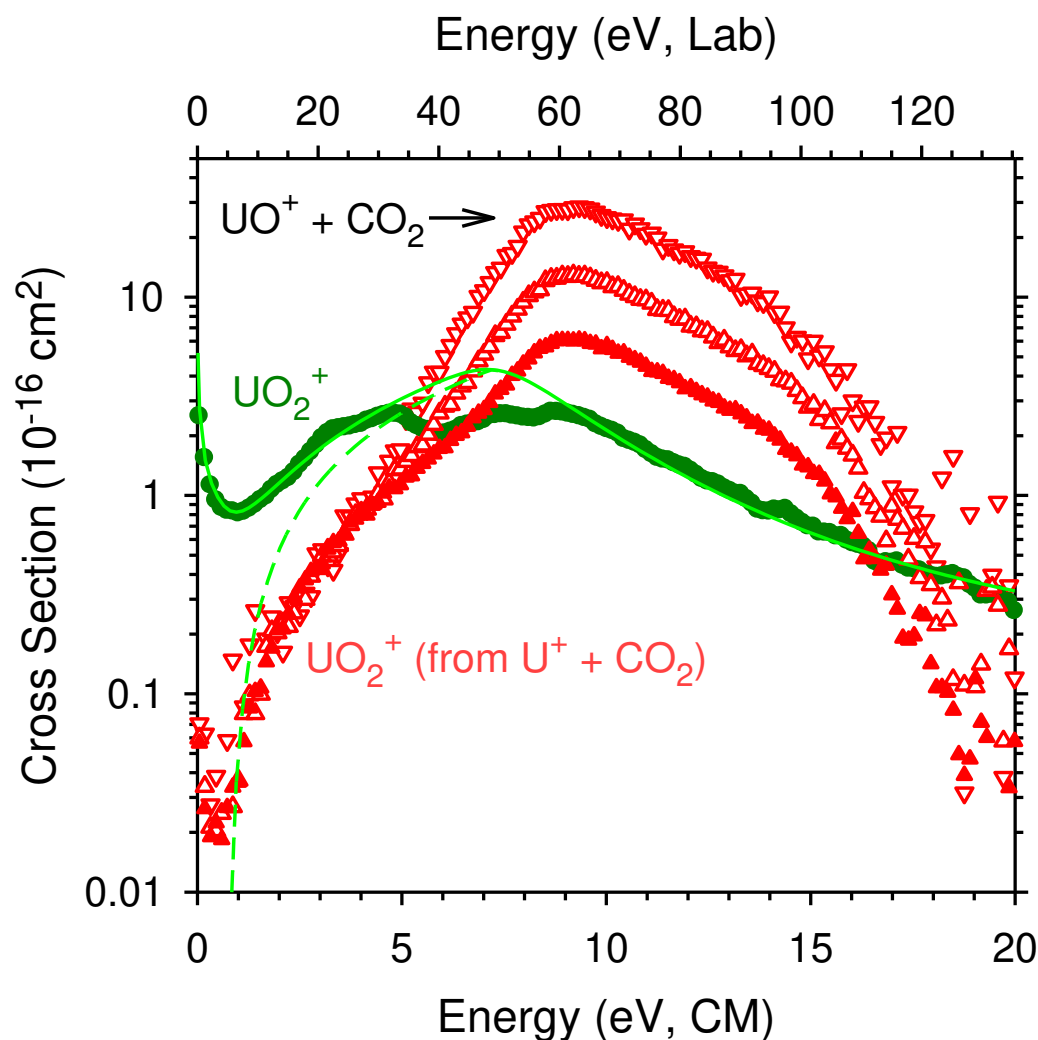


Figure 5.  $\text{UO}_2^+$  product ion cross section for the reaction of  $\text{UO}^+ + \text{CO}_2$  as a function of ion kinetic energy in the center-of-mass (lower x-axis) and laboratory (upper x-axis) frames. The resulting  $\text{UO}_2^+$  cross section is shown by green circles. The model of the endothermic feature of the  $\text{UO}_2^+$  cross section using Eq. 1 is shown by the dashed green line. The full green line shows this model summed with a model for the exothermic reaction convoluted over the reactant internal and kinetic energies. The pressure dependent  $\text{UO}_2^+$  cross sections from the reaction of  $\text{U}^+ + \text{CO}_2$  (treated as though the primary  $\text{UO}^+$  product is the reactant) are represented by the inverted red triangles (0.4 mTorr), upright red triangles (0.2 mTorr), and filled upright red triangles (0.1 mTorr).

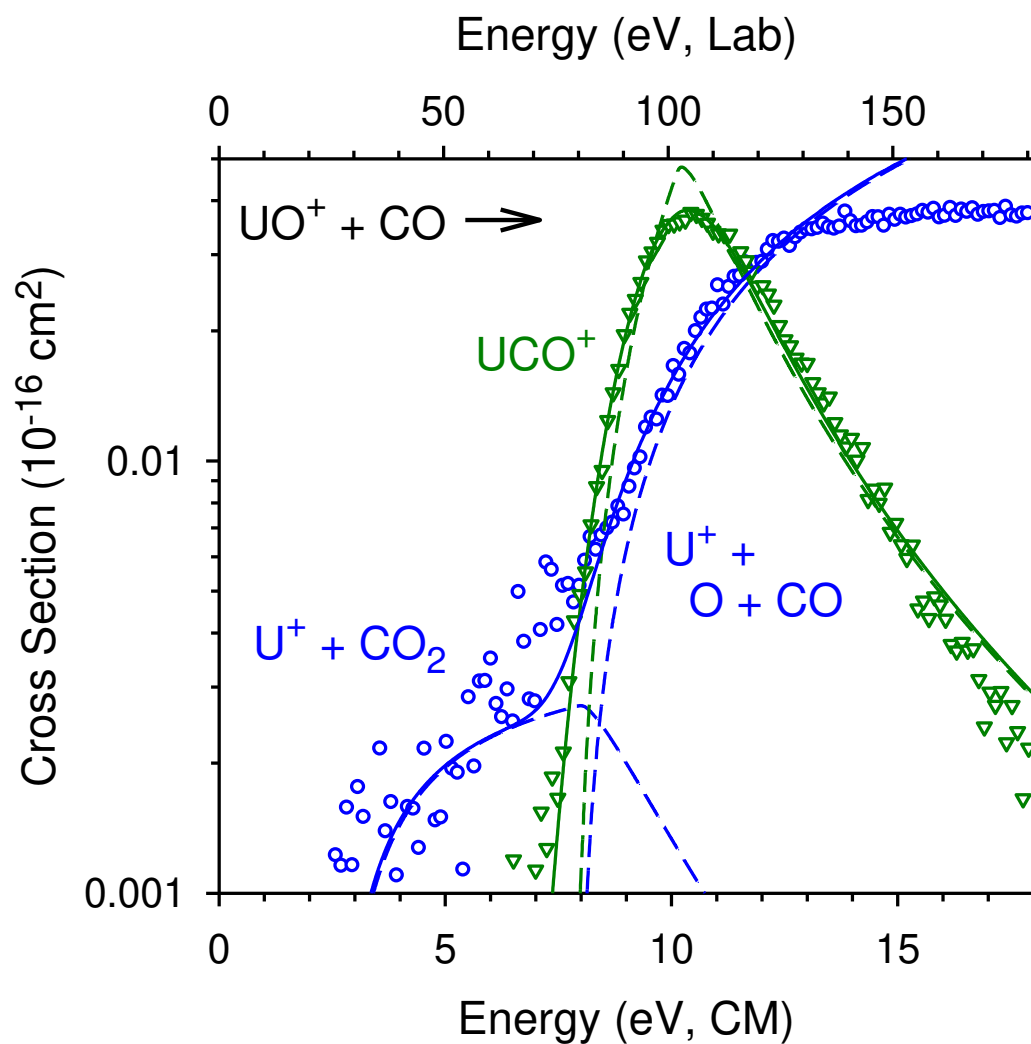


Figure 6. Product ion cross sections for the reaction of  $\text{UO}^+ + \text{CO}$  as a function of ion kinetic energy in the center-of-mass (lower x-axis) and laboratory (upper x-axis) frames. Symbols show cross sections for  $\text{U}^+$  (blue circles) and  $\text{UCO}^+$  (green inverted triangles). The models of both reactions using Eq. 1 are shown convoluted over the reactant internal and kinetic energies (solid lines) and unconvoluted (dashed lines). The low energy and high energy features of the  $\text{U}^+$  cross section were modeled independently (dashed blue lines). The sum of the convoluted models is shown by the solid blue line.